ISSN (Print) 1598-5385
ISSN (Online) 2233-6648
≪연구논문≫ Journal of the Korean Magnetics Society 36(2), 149-164 (2026) https://doi.org/10.4283/JKMS.2026.36.2.149

Topology and Parametric Two-Stage Optimization Design Process of Rotor Notches to Minimize Cogging Torque

Jung Hyun Choi, Tae-Gun Lee, Ji-Hoon Lee, Ye-Na Bae, and Myung-Seop Lim*
Department of Automotive Engineering (Automotive-Computer Convergence), Hanyang University, Seoul 04763, South Korea

(Received 17 March 2026, Received in final form 4 May 2026, Accepted 6 May 2026)

The increasing adoption of electric vehicles and sustainable mobility technologies has intensified the demand for high-speed, high-voltage permanent magnet synchronous machines. At elevated operating speeds, torque ripple is a critical performance concern because it induces vibration and noise, and cogging torque is one of its principal contributors. Conventional cogging torque mitigation techniques, such as skewing, magnet shaping, and slot-opening modification, often introduce trade-offs in manufacturability or torque capability. This paper proposes a two-stage rotor notch optimization approach to reduce cogging torque with minimal performance compromise. In the first stage, topology optimization identifies an effective notch shape within predefined regions, which is subsequently parameterized and refined through parametric shape optimization. The proposed method is validated through comparison with conventional parametric optimization and a baseline design, demonstrating superior cogging torque reduction while satisfying rated torque capability and mechanical stress limits.

Keywords : topology optimization, parametric optimization, cogging torque, interior permanent magnet synchronous motor, rotor notch design

코깅 토크 최소화를 위한 회전자 노치의 위상최적화-파라매트릭 2단계 최적 설계 기법

최정현 · 이태건 · 이지훈 · 배예나 · 임명섭*
한양대학교 미래자동차공학과(미래자동차-SW융합전공), 서울시 왕십리로, 222, 04763

(2026년 3월 17일 받음, 2026년 5월 4일 최종수정본 받음, 2026년 5월 6일 게재확정)

전기차 및 전동화 기술의 확산으로 고속 및 고전압 영구자석 동기 전동기에 대한 요구가 지속적으로 증가하고 있다. 고속 운전 조건에서는 진동 및 소음을 유발하는 토크 리플이 주요한 성능 문제로 작용하며, 이 중 코깅 토크는 대표적인 원인 중 하나이다. 스큐, 자석 형상 변경, 슬롯 개구부 수정과 같은 기존의 코깅 토크 저감 기법들은 제조성 저하 또는 토크 성능 감소를 수반해야 한다. 본 논문에서는 토크 성능 저하를 최소화하면서 코깅 토크를 줄이기 위한 2단계 회전자 노치 최적화 기법을 제안한다. 첫 단계에서는 위상 최적화를 통해 사전에 정의된 영역 내에서 효과적인 노치 형상을 도출하고, 다음 단계에서는 파라매트릭 최적화를 수행한다. 제안된 방법은 기준 모델 및 기존 파라메트릭 최적화 기법과의 비교를 통해 검증되었으며, 정격 토크 성능과 기계 강성 제약 조건을 만족하면서도 우수한 코깅 토크 저감 효과를 달성함을 확인하였다.

주제어 : 위상최적화, 파라매트릭 최적화, 코깅 토크, 매입형 영구자석 동기전동기, 회전자 노치 설계

*Corresponding author: Tel: +82-2-2220-0436, Fax: + 82-2-2220-4465, e-mail: myungseop@hanyang.ac.kr

I. Introduction

The global transition toward sustainable electrification has accelerated the development of high-performance electrical machines with stringent requirements on efficiency, reliability, and power density. High-speed, high-voltage interior permanent magnet synchronous machines (IPMSMs) have emerged as a key technology for electric vehicles, aerospace systems, and other advanced electromechanical applications. Although high operating speeds increase power density, they simultaneously intensify electromagnetic and mechanical interactions, resulting in elevated vibration, acoustic noise.

Among the various sources of torque ripple, cogging torque is a dominant component [1]. It arises from the interaction between rotor-mounted permanent magnets and stator slotting and is attributed to the spatial variation of airgap reluctance during rotor rotation. Cogging torque is inherently load-independent and exists over the entire operating speed range. In high-speed machines, its detrimental effects become more pronounced in torque ripple, thereby amplifying vibration, acoustic noise [2]. Therefore, effective mitigation of cogging torque is essential to ensure smooth and reliable operation of high-speed IPMSMs.

Various approaches have been proposed to reduce cogging torque, including rotor skewing, magnet shaping, and slot-opening modification [3-5]. Although these methods can effectively suppress torque ripple, they often involve trade-offs in manufacturability, electromagnetic performance, or torque capability. Rotor notching provides an alternative solution by locally modifying the rotor surface to alter the airgap reluctance distribution, thereby directly addressing the primary source of cogging torque. However, identifying an optimal notch geometry remains a challenging task. Conventional notch designs typically rely on predefined geometric configurations or designer experience, which may not guarantee optimal performance.

In addition to geometric optimization approaches, recent studies have emphasized the importance of robustness against manufacturing tolerances and assembly imperfections in cogging torque reduction. It has been reported that unavoidable variations in permanent magnet properties, stator slot geometry, and assembly positioning can introduce additional harmonic components in cogging torque, significantly degrading the performance of an optimized design under ideal conditions.

To address these issues, several robust design methodologies have been proposed. Sensitivity-based analyses and worst-case evaluation techniques have been utilized to identify the influence of parameter uncertainties on cogging torque harmonics and to derive inherently robust design configurations. Furthermore, robust design optimization (RDO) frameworks incorporating statistical variation and manufacturing tolerances have been developed to minimize both the mean and variance of cogging torque [6,7].

Despite these efforts, existing robust design approaches are typically confined to predefined geometric parameter spaces, limiting their ability to explore fundamentally different rotor topologies. As a result, the achievable performance improvement is inherently restricted by the initial design assumptions.

To address this limitation, this paper proposes a two-stage rotor notch optimization framework for cogging torque reduction in high-speed IPMSMs. The core contribution of this research lies in the synergy between unconstrained topology exploration and manufacturing-oriented design variable refinement. Conventional approaches are constrained by predefined geometric primitives and limited design variable variations, restricting the accessible design space. In contrast, the proposed two-stage framework first enables the exploration of a wide range of rotor notch geometries without predefined shape constraints through topology optimization, allowing the identification of electromagnetically sensitive regions and non-parametric flux-guiding geometries that reshape local magnetic flux paths. These features are subsequently converted into a manufacturable and optimized geometry through design variable refinement. In the first stage, topology optimization is employed to explore unconstrained free-form notch geometries and identify configurations with significant influence on cogging torque reduction. In the second stage, the topology-optimized geometry is parameterized into a manufacturable representation and further refined using surrogate-assisted parametric optimization. The optimization objective is to minimize cogging torque while preserving torque capability.

The effectiveness of the proposed framework is validated through comparative analysis with a baseline design and conventional parametric optimization approaches. The results demonstrate improved cogging torque reduction with minimal compromise in torque performance.

II. Theory and Technical Background

1. Cogging Torque Fundamentals and Theory

Cogging torque in IPMSMs originates from the interaction between rotor-mounted permanent magnets and the stator slot structure. As the rotor rotates, spatial variation of airgap reluctance due to slotting causes periodic

changes in magnetic energy, generating a position-dependent torque even under no-load conditions. In high-speed IPMSMs, this torque disturbance can contribute to vibration and acoustic noise.

The origin of cogging torque is explained by the variation of magnetic energy stored in the airgap. Assuming the magnetomotive force (MMF) is generated by the permanent magnets (PM) and that airgap reluctance variation is represented by relative airgap permeance, the PM MMF distribution is expressed as

$$F(\theta,\alpha)=\sum_{m=1}^{\infty}\left[F_{a,mN_p}\cos(mN_p(\theta+\alpha))+F_{b,mN_p}\sin(mN_p(\theta+\alpha))\right] \quad (1)$$

where θ is the spatial angular coordinate in the stator reference frame and α denotes the rotor mechanical position. The variable N_p denotes the total number of rotor poles, and m is a positive integer defining the rotor spatial harmonic index. The coefficients $F_{a,mNp}$ and $F_{b,mNp}$ are Fourier coefficient corresponding to the cosine and sine components of the rotor MMF harmonic of order mN_p, respectively.

The relative airgap permeance is similarly expanded as

$$G(\theta)=G_0+\sum_{n=1}^{\infty}\left[G_{a,nN_s}\cos(nN_s\theta)+G_{b,nN_s}\sin(nN_s\theta)\right] \quad (2)$$

where G_0 is the average airgap permeance corresponding to the effective uniform airgap length. The quantity N_s denotes the number of stator slots, and n is a positive integer representing the stator spatial harmonic index. The coefficients $G_{a,mNs}$ and $G_{b,mNs}$ are Fourier coefficients associated with the cosine and sine components of the slot-induced permeance harmonic of order nN_s.

Due to stator slotting, the airgap permeance varies periodically with angular position. As the rotor magnetic field traverses this nonuniform distribution, the flux overlaps between magnets and stator teeth changes, producing periodic variations in stored magnetic energy. Neglecting energy changes in the core and magnets relative to the airgap, the magnetostatic energy is expressed as

$$W(\alpha)=\frac{1}{2\mu_0}\int_V G^2(\theta)F^2(\theta,\alpha)dV \quad (3)$$

where μ_0 is the vacuum permeability. Assuming a cylindrical airgap region, equation (3) simplifies to

$$W(\alpha)=K\int_0^{2\pi}G^2(\theta)F^2(\theta,\alpha)d\theta \quad (4)$$

with

$$K=\frac{L_{stk}}{4\mu_0}\left(R_2^2-R_1^2\right) \quad (5)$$

where L_{stk} is the stack length, R_1, and R_2 denote the inner and outer airgap radius, and K encapsulates the physical dimension of the machine that scale the stored magnetic energy. Since cogging torque arises solely from magnetic energy variation with rotor position, it is defined as

$$T_{cog}(\alpha)=-K\frac{\partial}{\partial\alpha}\int_0^{2\pi}G^2(\theta)F^2(\theta,\alpha)d\theta \quad (6)$$

Because both $G(\theta)$ and $F(\theta, \alpha)$ are spatially periodic functions represented by Fourier series in equations (1) and (2), their interaction inside the integral is governed by harmonic orthogonality. Over one mechanical period, the integral evaluates as

$$\int_0^{2\pi}G^2(\theta)F^2(\theta,\alpha)d\theta=\begin{cases}0, & nN_s\neq mN_p\\ \neq 0, & nN_s=mN_p\end{cases} \quad (7)$$

Therefore, a nonzero contribution occurs only when their spatial frequencies satisfy

$$nN_s=mN_p \quad (8)$$

which represents the harmonic coupling condition. The lowest harmonic order fulfilling (8) is determined by the least common multiple of N_p and N_s

$$z=LCM(N_s,N_p) \quad (9)$$

Consequently, the cogging torque waveform can be expressed as a summation of harmonics at integer multiples of z

$$T_{cog}(\alpha)=\pi zK\sum_{l=1}^{\infty}l(G_{a,lz}F_{a,lz})\sin(lz\alpha) \quad (10)$$

This formulation indicates that the amplitude of each cogging torque harmonic is proportional to the product $G_{a,lz}F_{a,lz}$. Since both permeance and MMF Fourier coefficients generally decrease with increasing harmonic order the product diminishes for larger l. Consequently, cogging torque is typically dominated by low-order harmonic components, while higher-order harmonics contribute progressively less. Therefore, effective cogging torque mitigation requires suppression of the dominant harmonic interactions between the rotor magnetic field and stator slotting [8].

2. Methods to Reduce Cogging Torque

Various techniques have been proposed to mitigate cogging torque by attenuating the spatial harmonic interaction between airgap permeance and the PM MMF. Since cogging torque originates from harmonic coupling that satisfies the spatial matching condition, mitigation strategies focus on reducing the specific harmonic com-

ponents responsible for this interaction rather than altering the average permeance or fundamental MMF.

Stator-side techniques target slot-induced permeance harmonics. Slot-opening modification is widely used, where the stator tooth geometry is tapered or chamfered to smooth airgap flux distribution. This approach reduces the magnitude of slot-related permeance harmonics while preserving average airgap characteristics. However, its applicability is limited by stator geometry design constraints, particularly in machines with predefined or standardized structures.

Rotor-side techniques weaken harmonic interaction from the rotating field. Rotor skewing axially offsets the rotor to cancel selected MMF harmonics through phase averaging. Although effective in reducing cogging torque, skewing generally decreases average torque and increases manufacturing complexity.

Modification of magnet geometric parameters, such as the pole arc ratio or surface chamfer, reshapes the MMF harmonic spectrum and suppresses targeted components contributing to cogging torque. However, such modifications may reduce effective magnet volume or alter magnetization distribution, potentially degrading torque capability and increasing manufacturing cost.

A more localized strategy involves direct modification of rotor surface geometry. Features such as notches are introduced to locally alter reluctance distribution and disrupt harmonic coupling between magnets and stator slots. Rotor notching has demonstrated strong potential for cogging torque reduction with minimal impact on the rated torque output [9]. Nevertheless, conventional notch designs rely on predefined geometries or designer experience, limiting their design flexibility and preventing systematic exploration of optimal configurations. These limitations motivate topology optimization-based rotor notch design methodologies.

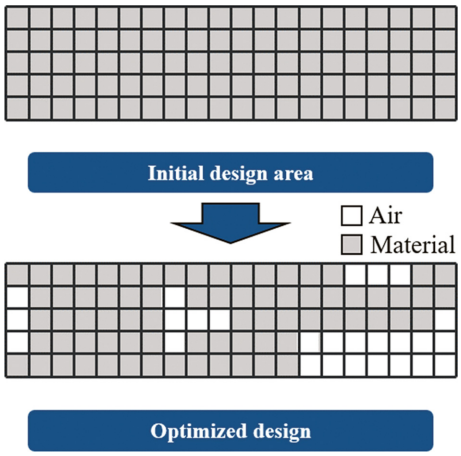

Fig. 1. (Color online) Topology optimization.

3. Topology Optimization Theory

Topology optimization determines the optimal material distribution within a design region without restricting geometry to predefined parameters as illustrated in Fig. 1. This capability enables discovery of non-intuitive geometries that influence electromagnetic phenomena such as cogging torque.

The material distribution within the design region is represented as a weighted sum of Gaussian basis functions, forming a continuous scalar field that defines the presence of material. Each Gaussian basis function is defined as a smooth, bell-shaped distribution

$$G_i(x,y) = A_i \exp\left(-\frac{(x-x_i)^2+(y-y_i)^2}{2\sigma_i^2}\right) \tag{11}$$

where A_i is the amplitude (weight), (x_i, y_i) is the center location, and σ_i controls the spatial spread of the function. Each function forms a smooth, bell-shaped surface in 3D space, and a circular contour due to radial symmetry in a

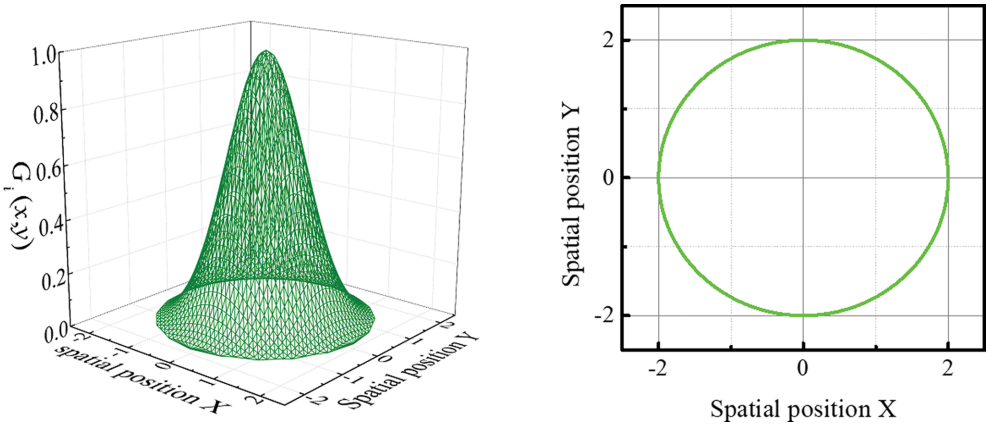

Fig. 2. (Color online) Gaussian basis function.

2D space, as illustrated in Fig. 2. For the purpose of simplicity, the Gaussian basis function will be represented in its 2D form.

A_i determines the amplitude of each Gaussian basis function, controlling the strength and sign of its local contribution. Positive values of A_i contribute to material retention, while negative values contribute to material removal in the surrounding region. In contrast, σ_i controls the spatial extent of its influence, determining how broadly each basis function affects the geometry. Together, these parameters define both the intensity and spatial distribution of the material field, enabling flexible modification of the rotor geometry with both global and localized shape variations, without reliance on predefined geometric constraints. The use of Gaussian basis functions is motivated by their smooth and localized characteristics. Their localized influence allows continuous control of material distribution within specific regions while maintaining overall geometric continuity. Compared to conventional parametric approaches based on predefined geometric primitives, the Gaussian-based representation enables complex geometries to be generated using a relatively small number of design variables, as each basis function influences a continuous region of the geometry. To illustrate this difference in design flexibility, Fig. 3 compares the Gaussian-based representation with a conventional parametric approach. In the Gaussian formulation, two overlapping basis functions provide smooth and continuous geometric control using only two design variables, even when the spatial locations and spreads of the Gaussian basis functions are fixed. By only adjusting the amplitudes, complex shapes can be generated through the superposition of their contributions. In contrast, achieving a comparable level of geometric flexibility with conventional parametric methods typically requires multiple independent variables to define individual geometric features and boundaries. This demonstrates that the Gaussian-based representation can achieve similar geometric expressiveness with a reduced number of design variables.

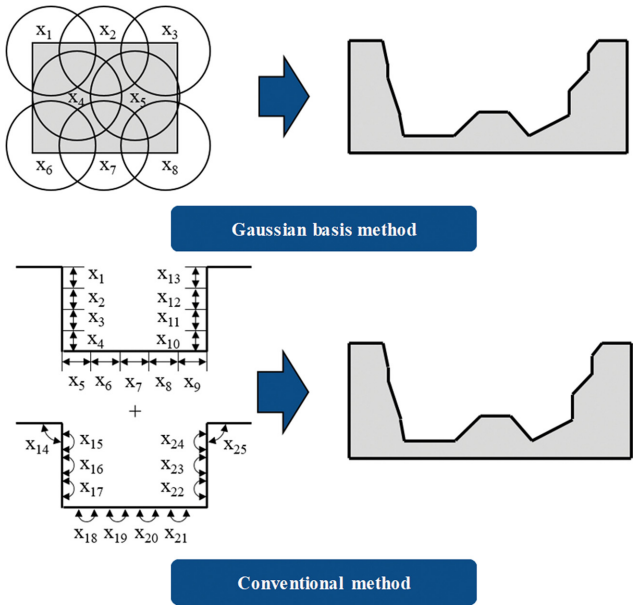

Fig. 3. (Color online) Comparison of the design variables: Gaussian basis vs conventional approach.

The degree of overlap between basis functions governs the scale of geometric modification, as shown in Fig. 4. Large overlap produces a broad and smoothly varying material field, enabling global geometric modifications and large-scale topology changes. In contrast, smaller overlap generates shaper spatial gradients, facilitating localized geometric modification and fine-scale shape refinement. This multiscale representation enables the optimization framework to explore both large-scale design variation and detailed geometric adjustments within a unified formulation.

A normalized Gaussian network (NGnet) aggregates Gaussian basis function contributions into a scalar field $y(x)$. Material is retained where $y(x) \geq 0$ and removed where $y(x) < 0$, producing a binary material distribution and illustrated in Fig. 5 [10-13]. In this way, the rotor geometry is defined implicitly from the scalar field rather

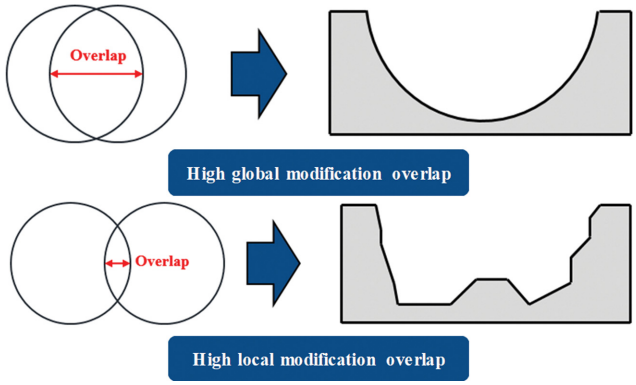

Fig. 4. (Color online) Gaussian surface overlap effects.

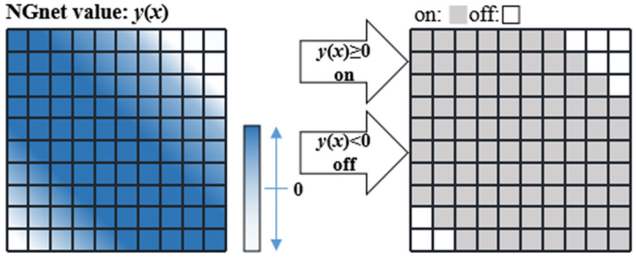

Fig. 5. (Color online) NGnet material distribution.

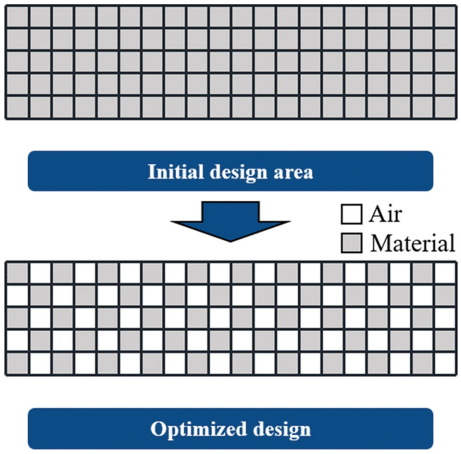

Fig. 6. (Color online) Checkerboard problem.

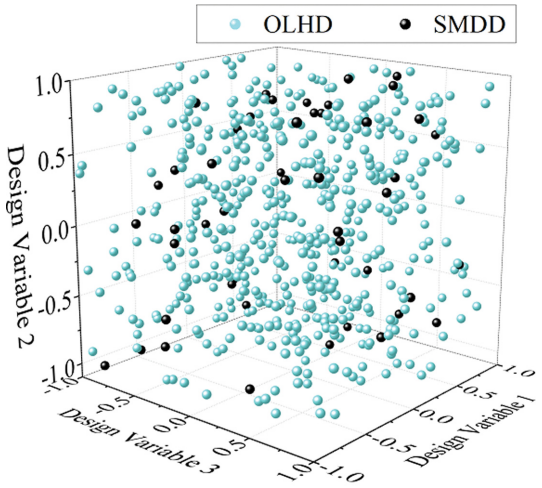

Fig. 7. (Color online) OLHD & SMDD.

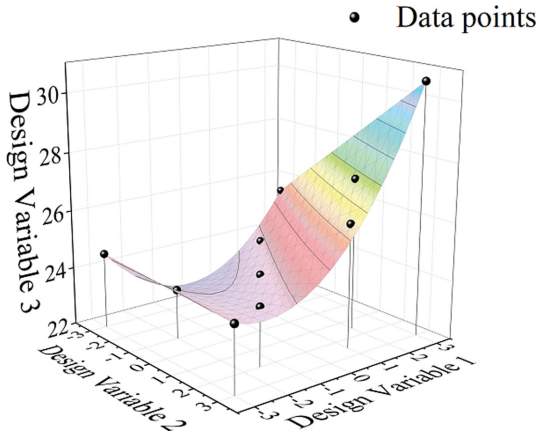

Fig. 8. (Color online) Kriging model.

than by explicit geometric boundaries. Gaussian basis function weights serve as design variables and are optimized using a genetic algorithm (GA). Candidate designs are evaluated using electromagnetic performance metrics, and evolutionary operations guide the search toward improved solutions.

Material distribution methods may produce checkerboard problem consisting of alternating solid and void regions Fig. 6. These nonphysical patterns arise from numerical instability, degrade structural integrity, and manufacturability. To suppress nonphysical patterns and ensure structural robustness, penalty terms and continuity constraints are incorporated into the optimization process. Increasing the number of Gaussian basis functions enhances geometric resolution but raises computational cost; therefore, a balance between design flexibility and efficiency is required.

Topology optimization identifies geometries with strong influence on cogging torque but often yields mesh-dependent shapes that are not directly manufacturable. Consequently, further refinement through parametric optimization is required.

4. Parametric Optimization Theory

Parametric optimization defines geometry using a finite set of design variables such as lengths, angles, and radius. By restricting the design space to manufacturable parameters, this approach is computationally efficient and compatible with production constraints.

In electric machine design, parametric optimization typically follows sensitivity analysis to identify variables with the greatest performance impact. A design of experiments (DoE) is then used to sample the parameter space systematically. In this work, an orthogonal latin hypercube design (OLHD) combined with sequential maximin distance design (SMDD) ensures uniform coverage of the design space Fig. 5 [14].

Data from the DoE are used to construct a surrogate model that approximates the relationship between geometric parameters and performance metrics. A Kriging model is employed due to its ability to represent nonlinear behavior by interpolating sampled data points (Fig. 8). The surrogate model reduces computational cost by enabling rapid evaluation of candidate designs without repeated finite element analysis (FEA) [15].

After surrogate model construction, a global optimization algorithm explores the parameter space. This paper employs GA because it efficiently handles nonlinear optimization landscapes using evolutionary operations such as selection, crossover, and mutation [16]. Iterative evolution of design parameters converges toward configurations that minimize cogging torque while satisfying performance constraints Fig. 9.

In the proposed framework, parametric optimization

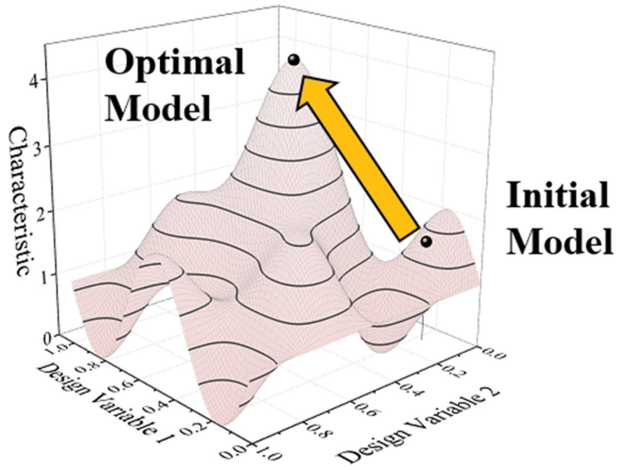

Fig. 9. (Color online) Optimization trajectory on surrogate model surface.

reconstructs the freeform geometry identified by topology optimization into a manufacturable rotor notch design while preserving performance benefits.

III. Design Methodology

1. Baseline Motor Characteristics

The baseline machine is a high-performance V-type IPMSM with 48 stator slots and 8 rotor poles and a stack length of 160 mm. The machine is rated at 200 kW with a rated speed of 7,000 rpm and a maximum speed of 21,000 rpm, representing high-speed and high-power-density applications.

Under a phase current limit of 280 A_{rms} and a DC-link voltage of 770 V, the baseline design produces a rated torque of 324 Nm. Under no-load conditions, the peak cogging torque is 4.25 Nm, which is significant for high-speed operation where periodic torque disturbances can amplify vibration and acoustic noise. The baseline geometry and specifications are summarized in Table I, and the corresponding geometry is shown in Fig. 10. The rated torque and cogging torque waveforms of the baseline model are shown in Fig. 11 and Fig. 12, respectively. The corresponding FFT of the cogging torque in Fig. 13 indicates that the 12th-order harmonic is dominant under no-load conditions. For the 48-slot, 8-pole IPMSM, the cogging torque periodicity is governed by the interaction between stator slots and rotor pole pairs. This results in 48 torque pulsations per mechanical revolution, which correspond to a 12th-order harmonic per

Table I. Baseline model specifications.

Parameter		Unit	Design Specification
Rated Operating Point	Torque	Nm	324
	Speed	rpm	7,000
Max Speed		rpm	21,000
Current Limit		A_{rms}	280
Voltage Limit		V_{DC}	770
Pole/Phase/Slot		-	8/3/48
Stack Length		-	1
Stator Outer Diameter		-	1.25
Core material		-	20PNX1150F
Permanent Magnet (N45H @60 °C)	Residual Flux Density	T	1.2852

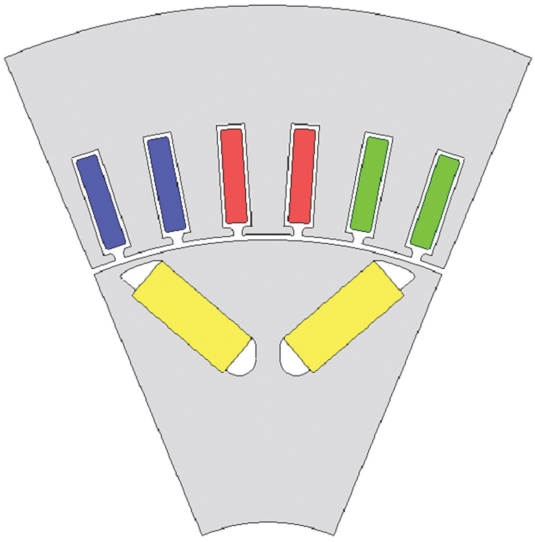

Fig. 10. (Color online) Baseline model.

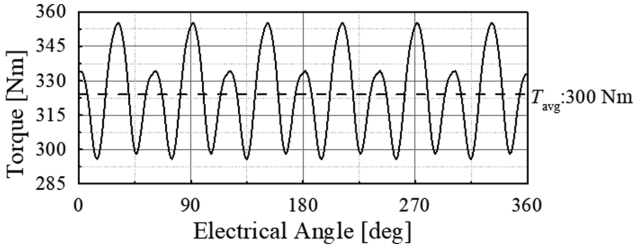

Fig. 11. Baseline model rated torque.

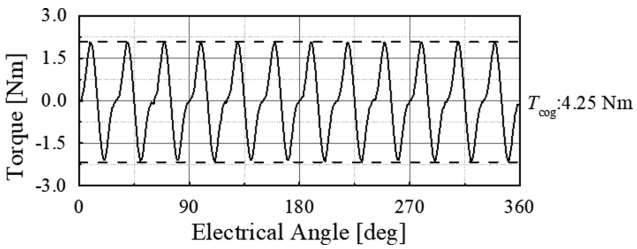

Fig. 12. Baseline model cogging torque.

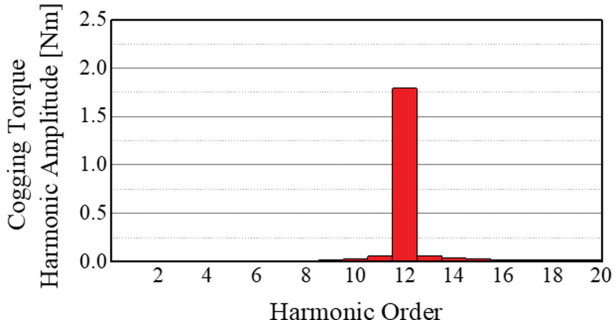

Fig. 13. (Color online) Baseline model cogging torque FFT.

electrical period due to the presence of four pole pairs. To establish the relationship between cogging torque and airgap flux density, the magnetic energy based cogging torque expression (6) can be alternatively expressed using the Maxwell stress tensor formulation, which provides a direct representation of torque in terms of airgap flux density as

$$T_{cog}(\alpha) = r_g^2 L_{stk} \int_0^{2\pi} \frac{B_r(\theta,\alpha), B_t(\theta,\alpha)}{\mu_0} d\theta \tag{12}$$

which can be equivalently written as

$$T(\alpha) = r_g^2 L_{stk} \int_0^{2\pi} P_t(\theta,\alpha) d\theta \tag{13}$$

where P_t (θ, α) is the tangential component of the Maxwell stress tensor derived from the airgap flux density components B_r and B_t which denotes the radial and tangential components of the airgap flux density. Based on this formulation, the cogging torque waveform is reconstructed by spatially integrating P_t at each rotor position. Fig. 14 compares the cogging torque obtained from the analytical method (Maxwell stress tensor formulation) with that obtained from FEA. The two results show excellent agreement, confirming that the cogging torque is accurately represented by the airgap flux density

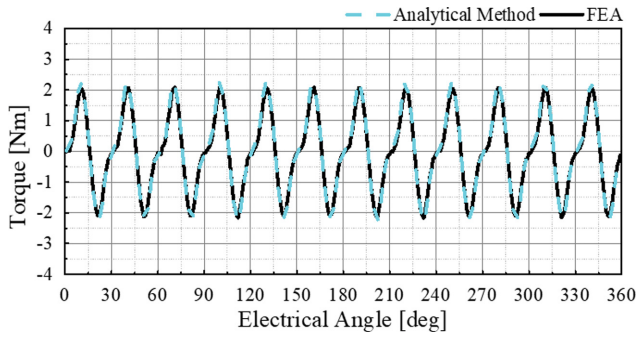

Fig. 14. (Color online) Comparison of the analytical method and FEA.

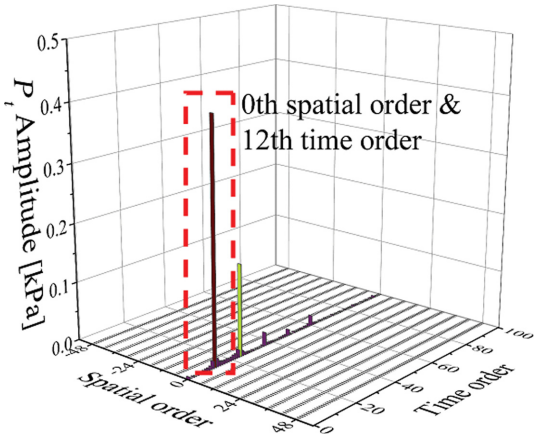

Fig. 15. (Color online) Harmonic amplitudes of tangential component of the Maxwell stress tensor (P_t).

through the Maxwell stress formulation. Since the torque is obtained by spatial integration of P_t, only the spatial 0^{th}-order component contributes to the resulting torque waveform. Therefore, the harmonic content of cogging torque is determined by the temporal harmonics of the spatially averaged P_t. Accordingly, Fig. 15 shows the temporal harmonic amplitudes of the spatially averaged P_t. It can be observed that the 12^{th}-order temporal harmonic exhibits the largest amplitude, followed by higher-order components such as the 24^{th} harmonic with a smaller magnitude. This confirms that the dominant cogging torque component originates from the spatial 0^{th}-order, temporal 12^{th}-order harmonic of P_t. Based on this analysis, the 12^{th}-order harmonic is identified as the primary contributor to cogging torque and its reduction is examined in the optimized designs in this study.

2. Conventional Optimization

To contextualize the performance of the proposed method, conventional parametric optimization was conducted using a trapezoidal notch geometry, which is widely adopted in practical machines due to its simplicity and manufacturability. The notch dimensions were defined as design variables and optimized within a restricted geometric parameter space.

To define the conventional optimization approach, a trapezoidal rotor notch geometry was adopted, which is widely used in practical machine design due to its simplicity and manufacturability. The notch dimensions were defined as design variables and optimized within a restricted geometric parameter space.

The conventional model considers only rotor notch modification coinciding with the proposed method, ensuring consistency in the design domain. The notch geometry is parametrized using predefined variables that control

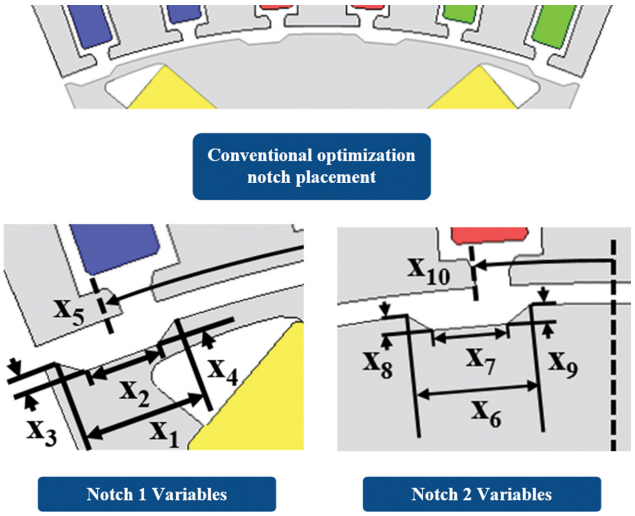

Fig. 16. (Color online) Conventional optimization design variables.

Table II. Design variables and min/max boundary of conventional optimization.

Variable	Unit	Upper Bound	Lower Bound
X_1	mm	2	0.5
X_2	mm	0.4	0.1
X_3	mm	0.7	0.1
X_4	mm	0.7	0.1
X_5	deg	20	18
X_6	mm	2	0.5
X_7	mm	0.4	0.1
X_8	mm	0.7	0.1
X_9	mm	0.7	0.1
X_{10}	deg	7	2

its position and dimensions along the rotor surface.

The notch locations and associated design variables are illustrated in Fig. 16, and the range of the variables is listed in Table II.

Nevertheless, because the geometry is constrained to a predefined trapezoidal form, the accessible design space remains restricted compared with freeform topology-derived geometries. Thus, this structural limitation may constrain the range of attainable harmonic suppression.

3. Notch Placement Method

Prior to topology optimization, a case study was conducted to identify rotor surface regions with strong influence on the dominant cogging torque harmonic. Optimization was restricted to areas that reduced the 12^{th}-order airgap flux density harmonic while satisfying mechanical stability requirements, thereby improving computational efficiency and design feasibility.

Small square notches were sequentially introduced on the rotor surface with angular positions defined relative to the rotor d-axis. The notches were applied symmetrically to maintain rotor balance. The angular search range was defined from 0^{o} to 21.5^{o}, as illustrated in Fig. 17 and Fig. 18. For each configuration, the airgap flux density was evaluated in the rotor reference frame, and a fast Fourier transform (FFT) was applied to extract harmonic components. The magnitude of the previously identified target harmonic was used as the performance metric.

By comparing the harmonic amplitude before and after localized material removal, the electromagnetic sensitiv-

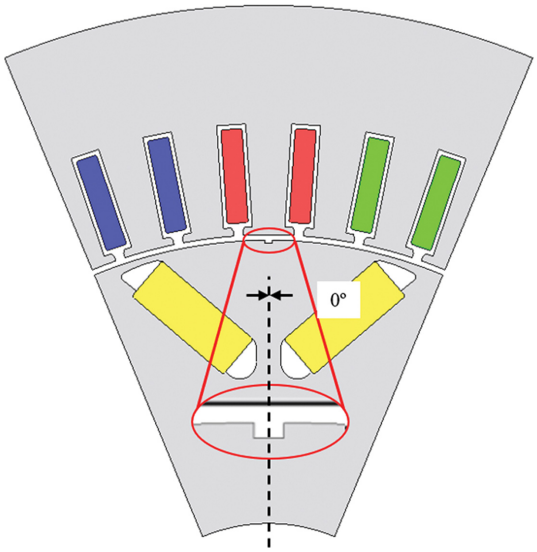

Fig. 17. (Color online) Lower bound notch placement.

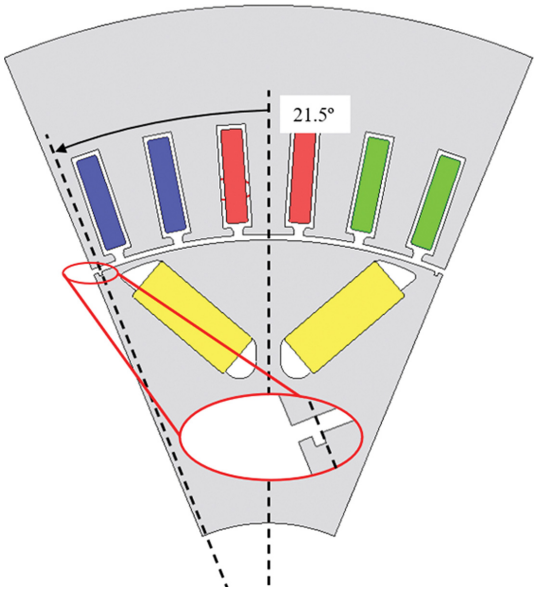

Fig. 18. (Color online) Upper bound notch placement.

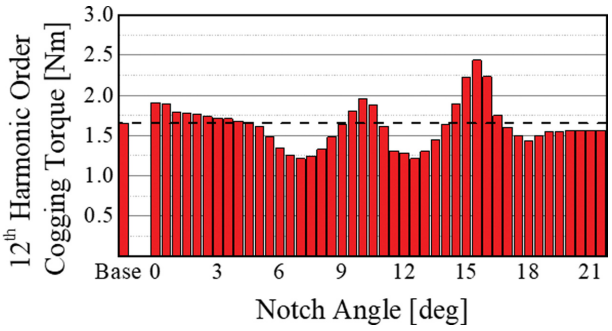

Fig. 19. (Color online) 12th-order cogging torque harmonic amplitude.

Fig 20. (Color online) 12th-order cogging torque harmonic reduced regions.

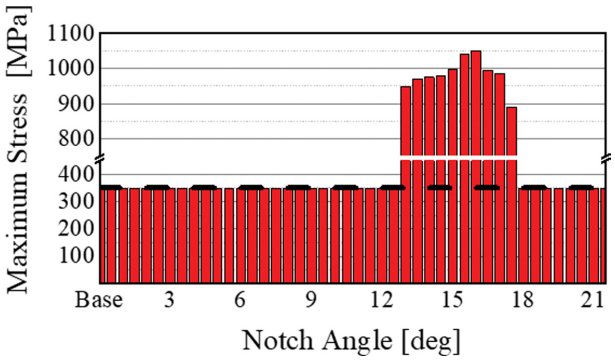

Fig 21. (Color online) Notch case study maximum von-Mises stress.

ity of each angular position was quantified. The resulting harmonic distribution is shown in Fig. 19, and regions exhibiting harmonic reduction are highlighted in Fig. 20.

To ensure structural integrity under high-speed operation, the maximum notch depth was limited to 0.7 mm, reflecting manufacturing and mechanical constraints. Structural feasibility was evaluated using von-Mises stress analysis under centrifugal loading. Regions failing to maintain a safety factor of 1.2 (equivalent to 350 MPa) were excluded. Maximum von-Mises stress distributions for each notch case are shown in Fig. 21, and structurally feasible and infeasible regions are summarized in Fig. 22.

Combining electromagnetic and structural constraints, three angular regions (5~9°, 11~12.5°, and 18~21.5° from the d-axis within one-eighth of the rotor segment) were

Fig. 22. (Color online) Structurally stable and unstable regions.

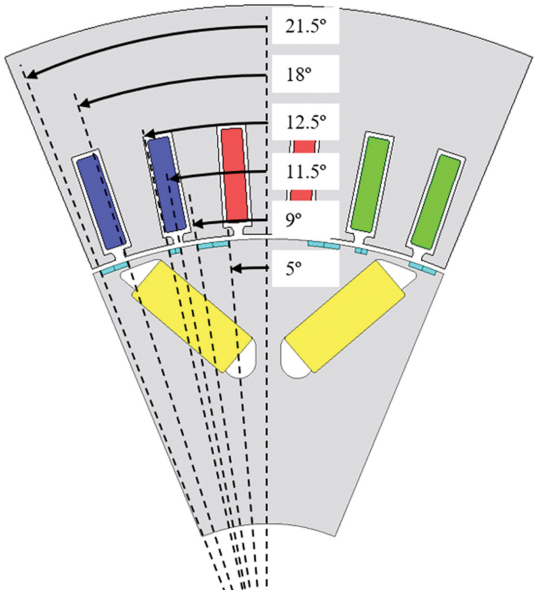

Fig. 23. (Color online) Topology optimization regions.

identified as suitable for optimization. These regions exhibited strong influence on the 12th-order harmonic while maintaining mechanical robustness. The resulting design domain for topology optimization is shown in Fig. 23.

4. Topology Optimization

Topology optimization was applied within the selected rotor regions to identify a freeform notch geometry that minimizes cogging torque without predefined shape constraints. The optimization domain is shown in Fig. 23, ensuring electromagnetic effectiveness and mechanical feasibility.

A Gaussian-based material distribution method was employed to represent the rotor geometry. The geometry was defined by superimposing multiple Gaussian basis functions, whose weights were treated as design variables to control the local material distribution within the optimization region. As described in Section II, the spread parameter governs the spatial extent of each basis function, while the weight determines its contribution to the material field. In this study, the spread parameters were fixed, and only the weights were treated as design variables to reduce the dimensionality of the optimization problem while retaining sufficient geometric flexibility.

By adjusting these weights, the optimization process enables flexible modification of the rotor geometry, allowing both global and localized shape variations to be explored without predefined geometric constraints. Specifically, positive weights promote material retention, while negative weights promote material removal. This formulation is particularly suitable for identifying rotor surface regions that strongly influence cogging torque. The Gaussian basis functions were arranged in three layers along the rotor periphery to provide sufficient geometric flexibility while maintaining computational efficiency. The mesh distribution was constructed with adequate spatial resolution to resolve the gradients of the Gaussian material field, ensuring accurate representation of geometric variations during optimization. This configuration enables both global and localized geometric modifications and the distribution of the Gaussian surfaces and the region mesh is illustrated in Fig. 24 and Fig. 25.

Each Gaussian function modifies underlying mesh elements to determine material retention or removal. Gaussian basis function weights serve as design variables and are optimized using a GA. The objective function is

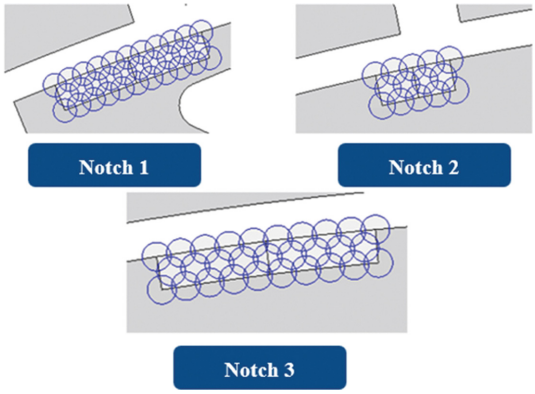

Fig. 24. (Color online) Gaussian surface distribution.

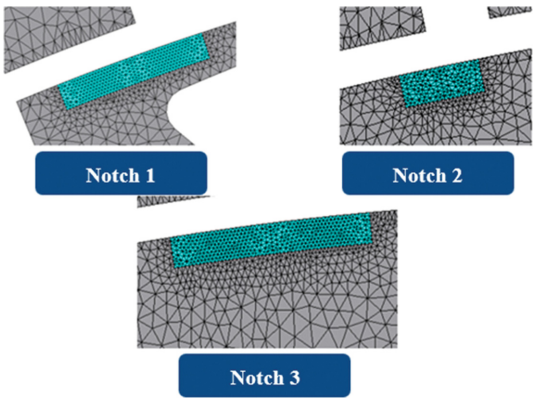

Fig. 25. (Color online) Region mesh distribution.

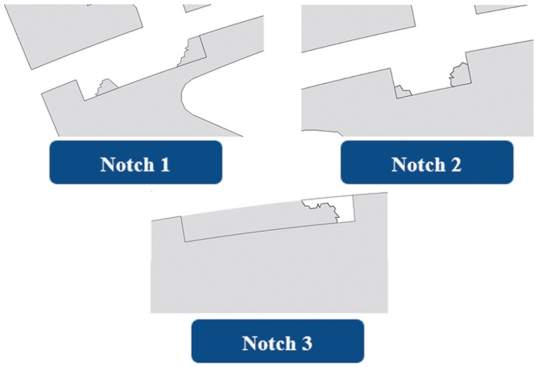

Fig. 26. (Color online) Topology optimization optimal model.

defined as cogging torque minimization, with emphasis on reducing the 12^{th}-order component. To preserve torque capability, a constraint requires the rated torque to remain above 97% of the baseline value 324 Nm.

The GA population size was set to 20 times the number of Gaussian basis functions to ensure sufficient design space exploration. The optimization was executed for 30 generations, providing convergence based on preliminary testing. Designs violating torque constraints or producing nonphysical geometries were penalized to ensure manufacturable solutions.

The topology optimization process produced an optimal freeform notch geometry within the defined regions as illustrated in Fig. 26. Although effective for cogging torque reduction, the resulting shape is mesh-dependent and not directly manufacturable, motivating subsequent parametric optimization.

5. Parametric Optimization

The parametric optimization stage reconstructs the topology-derived geometry into a smooth and manufacturable notch configuration while preserving the cogging torque reduction mechanism. The three notch regions (Notch 1-3) are defined at the same locations identified during the topology optimization stage, where dominant geometric notches contributing to cogging torque reduction were observed. By retaining these physically significant regions, the parametric model maintains the essential magnetic interaction characteristics while enabling geometric regularization.

Continuous boundaries and standard geometric primitives are employed to ensure manufacturability. Owing to the geometric irregularity of the topology-derived contour, forty design parameters are introduced to achieve sufficient geometric fidelity. These parameters define the notch length, angular span, and angular position. The selected number of variables provides adequate flexibil-

ity to approximate both the regularized geometry and its ±10% inward and outward offset variations, while maintaining computational efficiency. The complete parameter definition is illustrated in Fig. 27.

Due to the nonlinear relationship between geometry and cogging torque, extensive design space sampling was required. Given the high dimensionality of the design space (40 variables), 20,000 data points were generated

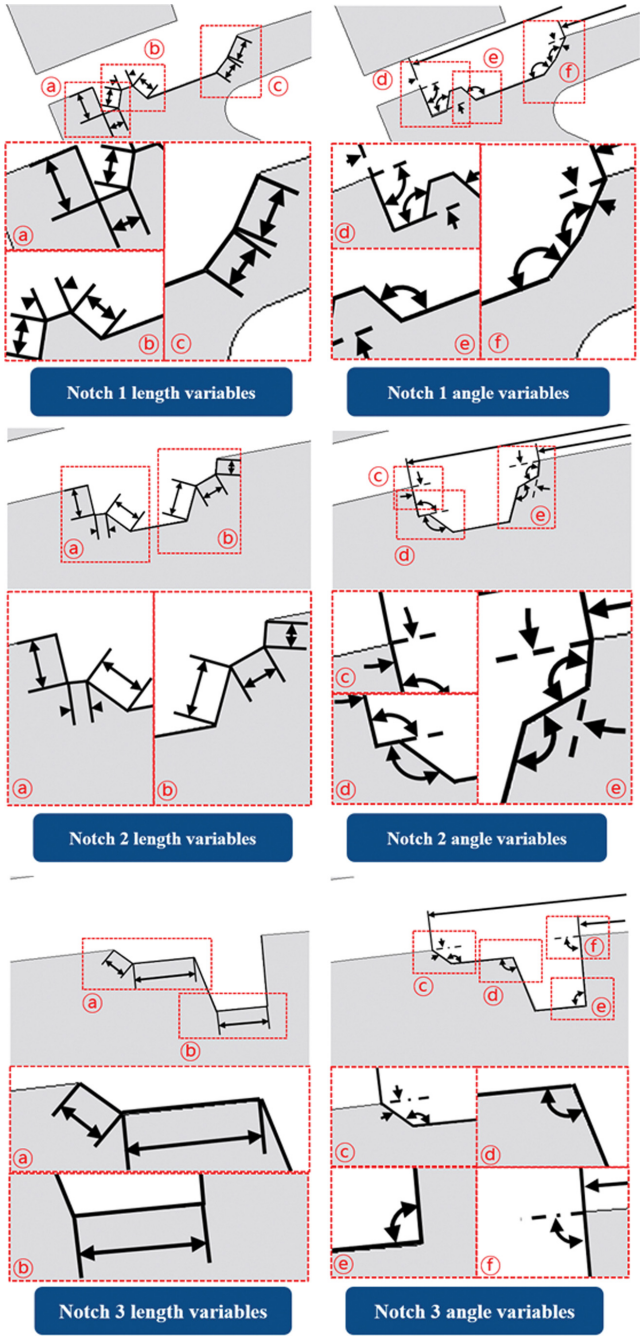

Fig. 27. (Color online) Parametric optimization design variables.

using an OLHD of 16,000 points combined with a SMDD of 4,000 points. Where each design was evaluated using FEA to compute cogging torque and the rated torque. This combined approach ensures efficient coverage of the design space, where OLHD provides a space-filling distribution with uniform global coverage, while SMDD sequentially adds samples that maximize the minimum distance between existing design points, thereby improving resolution in sparsely sampled regions. To assess whether the sampling is sufficient to accurately model the nonlinear relationship between the design variables and performance, the surrogate model was evaluated using normalized root mean square error (NRMSE), which quantifies the deviation between predicted and actual values.

The dataset was used to construct a Kriging surrogate model for performance prediction. Model accuracy was assessed using NRMSE

$$\mathrm{NRMSE} = \frac{1}{Y_{\max} - Y_{\min}} \sqrt{\frac{\sum_{i=1}^{N} (Y_i - \hat{Y}_i)^2}{N}} \tag{14}$$

where $Y_{\max}$, $Y_{\min}$ denote the maximum and minimum values of the observed data, and Y_i and $\hat{Y}_i$ represents actual and predicted responses, respectively. To evaluate the predictive capability of the Kriging surrogate model, a k-fold cross-validation procedure was performed. In this approach, the dataset is divided into multiple subsets of 10%, and the model is repeatedly trained on a portion of the data while the remaining subset is used for validation. This process allows the model's generalization performance to be assessed across different data partitions. Cross-validation does not prevent overfitting directly; however, it is effective in evaluating whether the model exhibits overfitting by comparing prediction errors on unseen data. The accuracy of the model was evaluated using NRMSE, which was found to be 6.08%. This low error rate indicates that the surrogate model effectively generalizes the complex relationship between the parameters and the characteristics, ensuring that the identified optimal design is a result of global trend identification rather than numerical overtraining.

A GA was applied to minimize cogging torque subject to the rated torque constraint

$$\text{Minimize: } J(s) = T_{cog}(s) \tag{15}$$

$$\text{Subject to: } g(s) = 314.3 - T_{\max} \le 0 \tag{16}$$

where s denotes the design variable vector. The optimization produced a smooth notch geometry that replicates the performance of the topology-optimized design while

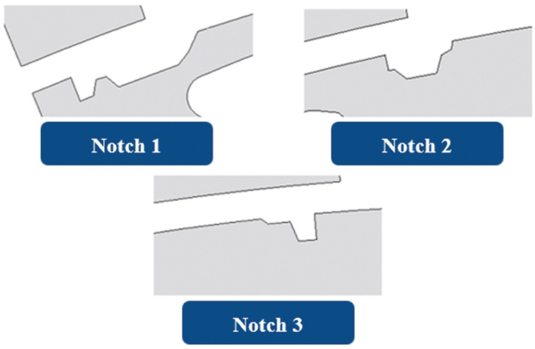

Fig. 28. (Color online) Parametric optimization optimal design.

satisfying manufacturing and torque constraints. The parametric optimization optimal design is shown in Fig. 28.

IV. Results and Discussion

1. Conventional Optimization Results

The conventional optimization approach exhibited superior performance relative to the baseline model. The conventional optimization notch produced a peak cogging torque of 3.16 Nm. The resulting cogging torque waveform is shown in Fig. 29.

The conventional optimization notch design yielded a rated torque of 321.75 Nm. The resulting rated torque waveform is shown in Fig. 30, which is lower than the baseline model. This reduction indicates that the predetermined notch geometry introduces airgap flux distortion that limits simultaneous cogging torque reduction and torque capability.

2. Topology Optimization Results

The topology-optimized design achieved a peak cogging torque of 1.66 Nm, corresponding to approximately a 60% reduction relative to the baseline value of 4.25 Nm. The resulting cogging torque waveform is shown in Fig. 31. This significant reduction confirms that the selected rotor regions exhibit strong electromagnetic influence, and that localized rotor surface modification effectively weakens the dominant 12^{th}-order cogging torque harmonic.

In addition to cogging torque reduction, the topology-optimized design satisfied the torque constraint imposed during optimization. The rated torque was 316.74 Nm, remaining within the allowable 3% reduction relative to the baseline, as shown in Fig. 32. This demonstrates that limited material removal from the rotor surface can substantially reduce cogging torque without severely compromising torque capability.

Despite favorable electromagnetic performance, the topology-optimized geometry contains irregular boundaries and mesh-dependent artifacts that prevent direct manufacturing. Therefore, the topology result serves as an idealized reference revealing geometry associated with cogging torque mitigation and guiding subsequent parametric reconstruction.

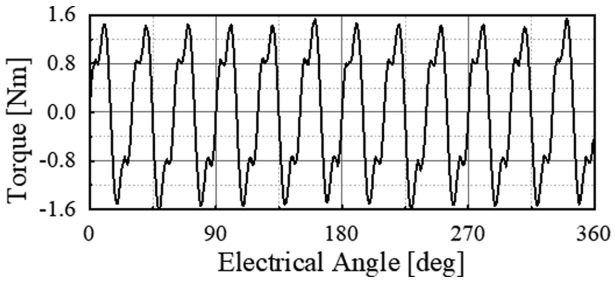

Fig. 29. Conventional parametric optimization cogging torque.

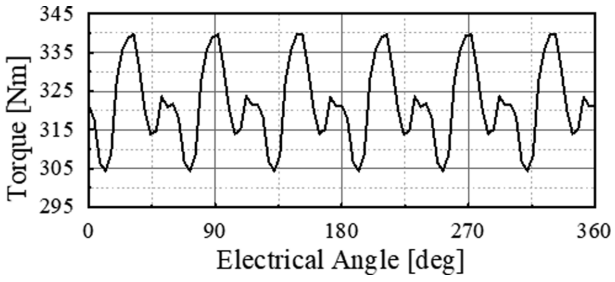

Fig. 30. Conventional optimization rated torque.

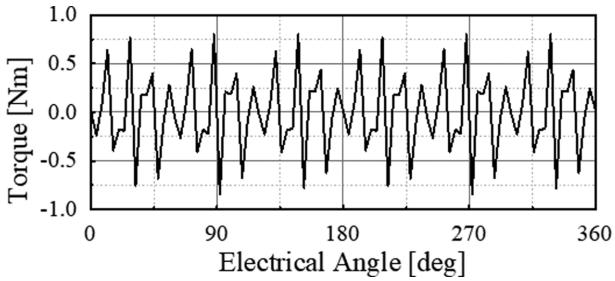

Fig. 31. Topology optimization cogging torque.

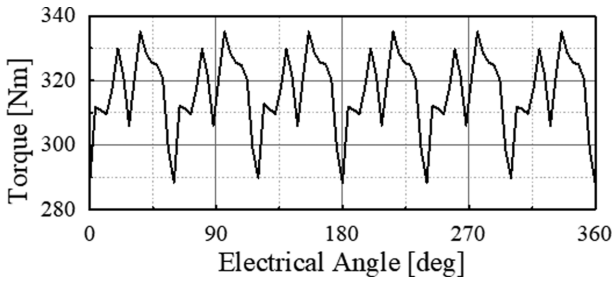

Fig. 32. Topology optimization rated torque.

3. Two-Stage Optimization Results

Following topology optimization, the freeform notch geometry was reconstructed into a smooth and manufacturable design using the parametric framework described in Section IV. Although the parametric model employs a larger number of design variables than conventional predefined shapes, this flexibility enables approximation of the dominant geometric characteristics identified by topology optimization.

The cogging torque and rated torque of the two-stage optimized design are shown in Fig. 33 and Fig. 34, respectively. The optimized model achieves a cogging torque of 1.32 Nm, representing a further reduction compared to the topology-optimized result (1.66 Nm) and the baseline model (4.25 Nm). This confirms that the proposed two-stage optimization framework enables additional reduction in cogging torque beyond topology optimization alone, and confirms it is the most effective method compared to other methods studied.

Independently, the rated torque of the optimized design is 317.45 Nm which remains, within the allowable 3% reduction from the baseline value of 324 Nm. This verifies that the improvement in cogging torque is achieved without significant degradation of torque performance.

Following the two-stage optimization, a final structural verification was performed. The peak von-Mises stress in the optimal model resulted in 341.75 MPa which remained below the 350 MPa threshold at the maximum operating speed of 21,000 rpm as illustrated in Fig. 35. This confirms that the high-performance magnetic geometry maintains a safety factor of 1.2.

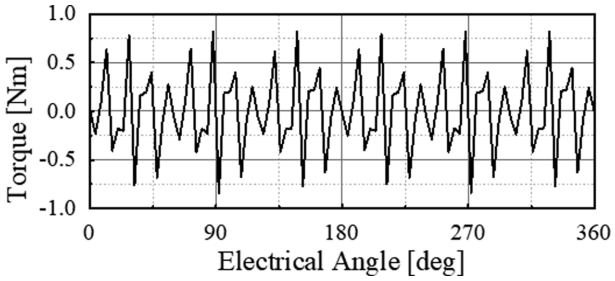

Fig. 33. Two-stage optimization cogging torque.

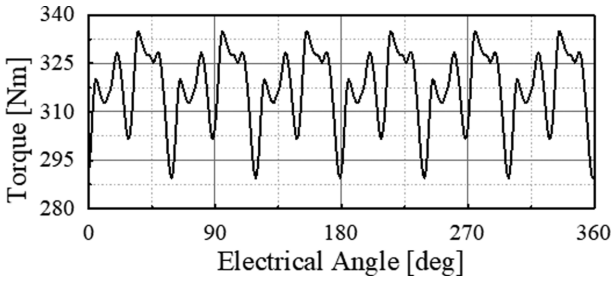

Fig. 34. Two-stage optimization rated torque.

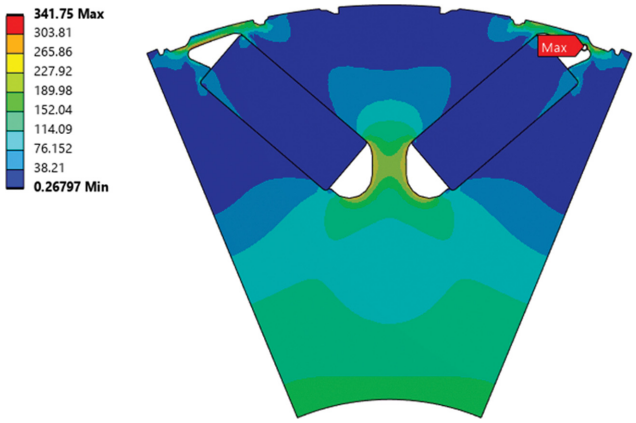

Fig. 35. (Color online) Two-stage optimization structural analysis.

4. Comparison of Methods

Performance metrics for all methods are summarized in Table III, and the corresponding optimal geometries are shown in Fig. 36. The rated torque waveforms are compared in Fig. 37, while the cogging torque waveforms and their harmonic amplitudes are presented in Fig. 38 and Fig. 39, respectively.

As shown in Fig. 38, all optimization methods achieve a reduction in cogging torque compared to the baseline model. The baseline exhibits a peak cogging torque of 4.25 Nm, which is reduced to 3.16 Nm using the conventional method. More substantial reductions are obtained through topology-based approaches, where the topology-only method decreases cogging torque to 1.66 Nm, and the proposed two-stage method further reduces it to 1.32 Nm, corresponding to the lowest value among all cases.

These results indicate that topology-driven geometry modification is more effective in suppressing cogging torque than conventional parametric approaches. The predefined notch geometry in the conventional method limits its ability to sufficiently alter the airgap permeance distribution, whereas topology optimization enables

Table III. Cogging torque and rated torque for each optimization method.

Method	Cogging Torque	Rated torque
	Nm	Nm
Base	4.25	324
Topology Optimization	1.66	316.74
Two-stage Optimization	1.32	317.45
Conventional Optimization	3.16	321.75

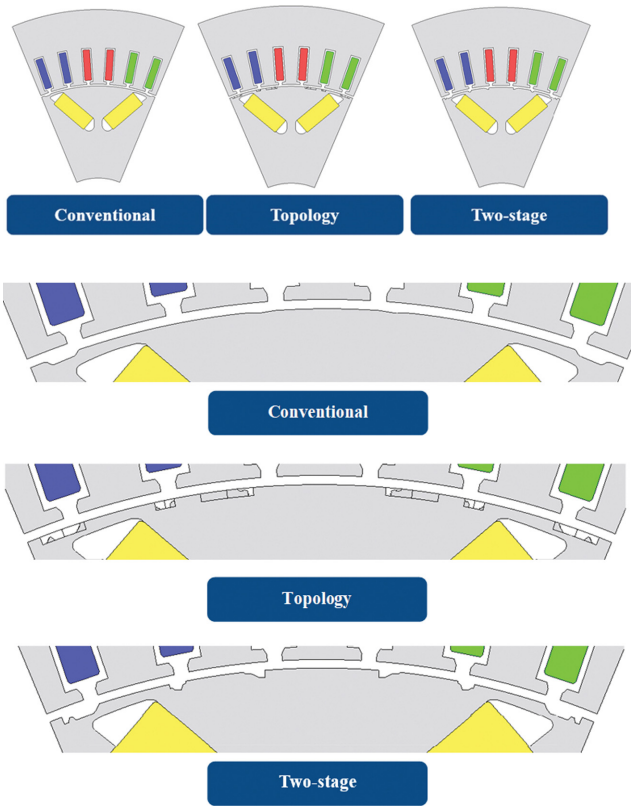

Fig. 36. (Color online) Optimal designs for each optimization method.

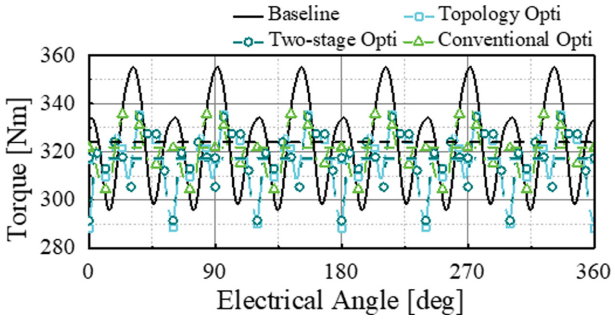

Fig. 37. (Color online) Comparison of rated torques.

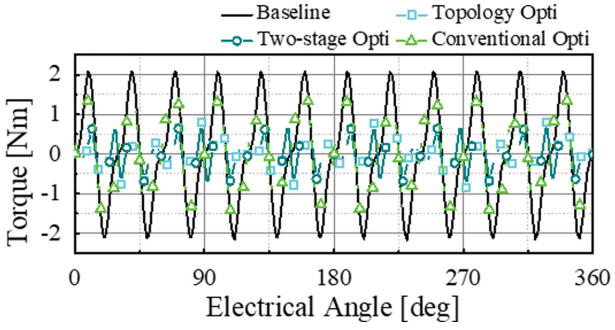

Fig. 38. (Color online) Comparison of cogging torques.

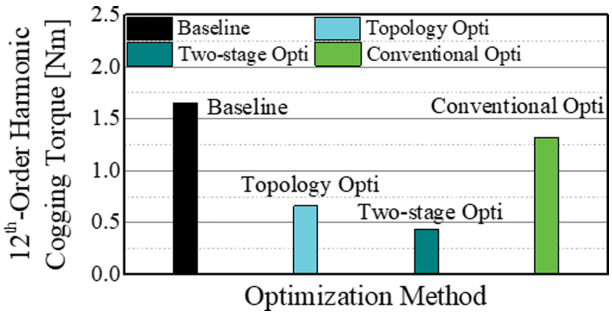

Fig. 39. (Color online) Comparison of cogging torque 12th harmonic order amplitude.

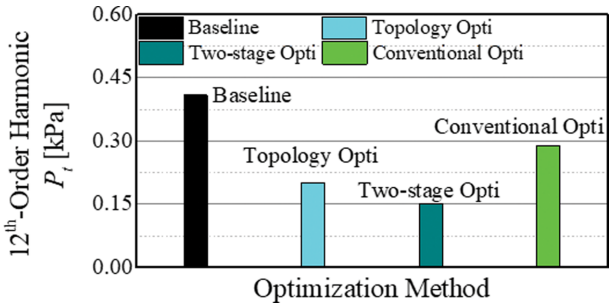

Fig. 40. (Color online) Comparison of Pt temporal 12th harmonic order amplitude.

more flexible modification of electromagnetically sensitive regions, leading to stronger attenuation of the dominant harmonic components, as shown in Fig. 39.

To further validate the relationship between airgap flux density and cogging torque, Fig. 40 presents the amplitude of the temporal 12th-order harmonic of the spatially averaged tangential Maxwell stress P_t for each method. A consistent trend is observed between Fig. 39 and Fig. 40, where the variation of the 12th-order harmonic obtained from FEA-based cogging torque closely follows that of the 12th-order component of P_t. This agreement confirms that the dominant cogging torque harmonic observed in FEA originates from the spatial 0th-order, temporal 12th-order component of P_t, as derived from the airgap flux density.

The rated torque values for all optimized models remain within the allowable 3% reduction constraint relative to the baseline. This confirms that the observed improvements in cogging torque are achieved without significant degradation of torque capability. Among the evaluated methods, the two-stage approach demonstrates the most effective performance, combining the design flexibility of topology optimization with subsequent geometric refinement to achieve the greatest reduction in cogging torque while satisfying the imposed design constraint.

V. Conclusion

This paper presented a two-stage rotor notch design methodology integrating topology optimization and parametric optimization for cogging torque reduction in high-speed IPMSMs. The topology optimization stage generated freeform rotor notch geometries that significantly reduced the dominant 12^{th}-order cogging torque harmonic without relying on predefined notch shapes. Although the resulting geometries are not directly manufacturable, they provide effective notch locations and geometric trends associated with cogging torque mitigation.

By reconstructing the topology-derived geometry using a high-dimensional parametric representation, a smooth and manufacturable notch design was obtained while preserving and maintaining electromagnetic performance. The final parametric design achieved substantially lower cogging torque than both the baseline machine and the conventional predefined-shape optimization approach. In contrast, the conventional method exhibited limited harmonic suppression capability, reflecting the constraints of shape-restricted design strategies.

The results indicate that topology optimization is effective for identifying performance-improving geometric shapes, while parametric optimization enables their practical realization and further refinement. The proposed two-stage framework therefore provides a systematic design approach that enhances cogging torque reduction without compromising torque capability.

Despite its effectiveness, the proposed method has limitations. Topology optimization is primarily suited to localized geometric modification and may exhibit sensitivity to mesh resolution and numerical artifacts. In addition, computational cost increases with higher resolution, limiting its application to large design domains.

Future work will consider multi-objective formulations incorporating torque ripple under load, core loss, and efficiency. Treating rated torque as a co-objective may further improve overall machine performance. Experimental validation of the optimized rotor notch geometry is also planned to confirm practical feasibility under real operating conditions.

Acknowledgements

This work was supported by the Hanwha Aerospace E-Drive Hub in 2025.

References

[1] X. Xu, B. Zhang, and J. Wu, Electronics **12**, 3499 (2023).
[2] U. Galfarsoro, J. Parra, A. McCloskey, S. Zarate, and X. Hernandez, Proc. IEEE Int. Workshop Electronics, Control, Measurement, Signals Their Application to Mechatronics (ECMSM), 1 (2017).
[3] I.-H. Jo, H.-W. Lee, G. Jeong, W.-Y. Ji, and C.-B. Park, IEEE Trans. Magn. **55**, 1 (2019).
[4] L. Dosiek and P. Pillay, IEEE Trans. Ind. Appl. **43**, 1565 (2007).
[5] M. Kashif and B. Singh, Proc. Int. Conf. Sustainable Energy and Future Electric Transportation (SEFET), 1 (2021).
[6] S.-G. Lee, S. Kim, J.-C. Park, M.-R. Park, T. H. Lee, and M.-S. Lim, IEEE Trans. Energy Convers. **35**, 2076 (2020).
[7] Y. Yang, N. Bianchi, G. Bramerdorfer, C. Zhang, and S. Zhang, IEEE Trans. Energy Convers. **36**, 2152 (2021).
[8] J. F. Gieras, J. C. Lai, and C. Wang, *Noise of Polyphase Electric Motors*, Taylor & Francis (2006) pp. 77~105.
[9] B. Wang, D. Wang, C. Peng, C. Wang, C. Xu, and X. Wang, IEEE Trans. Ind. Electron. **71**, 5519 (2024).
[10] M. P. Bendsøe and O. Sigmund, *Topology Optimization: Theory, Methods, and Applications*, Springer (2019) pp. 2~9, 298~303.
[11] X. He, L. Yan, P. Xiang, N. Du, X. Liu, I.-M. Chen, and H. Hu, IEEE/ASME Trans. Mechatronics **30**, 436 (2025).
[12] Y. Li, L. Liu, S. Yang, Z. Ren, and Y. Ma, IEEE Trans. Magn. **56**, 1 (2020).
[13] B. Ullah, Siraj-ul-Islam, Z. Ullah, and W. Khan, Comput. Math. Appl. **99**, 99 (2021).
[14] A. Afzal, K.-Y. Kim, and J. Seo, Int. J. Fluid Mach. Syst. **10**, 240 (2017).
[15] S. Jeong, M. Murayama, and K. Yamamoto, J. Aircraft **42**, 1375 (2005).
[16] R. Xu and W. Tong, CES Trans. Electr. Mach. Syst. **6**, 352 (2022).